scientific reports

OPEN

Hyaluronic acid dissolving microneedle patch-assisted acupoint transdermal delivery of triptolide for effective rheumatoid arthritis treatment

Siyao Li[1], Quanlong Chen[1], Yanglin Zhang[1], Di Wang[1], Huiling Hu[1], Jingjing Li[2]✉, Chen Zhang[1]✉ & Jinming Zhang[1]✉

Triptolide (TP), a major active component of the herb *Tripterygium wilfordii* Hook F, has been shown excellent pharmacological effects on rheumatoid arthritis. However, TP is prone to causing severe organ toxicity, which limits its clinical application. In recent years, microneedle technology has provided a new option for the treatment of arthritis due to its advantages of efficient local transdermal drug delivery. In this study, we constructed a microneedle platform to deliver TP locally to the joints, thereby enhancing TP penetration and reducing systemic toxicity. Additionally, we investigated whether acupoint drug delivery can produce a synergistic effect of needles and drugs. First, TP was loaded into microneedles using polyvinylpyrrolidone and hyaluronic acid as matrix materials. Next, we established a rat adjuvant-induced arthritis (AIA) model to evaluate the therapeutic effect of TP-loaded microneedles. The experiments showed that TP-loaded microneedles alleviated the AIA rats' inflammatory response, joint swelling, and bone erosion. However, there was no significant difference in the therapeutic effect observed in the acupoint and non-acupoint administration groups. In conclusion, TP-loaded microneedles have the advantages of safety, convenience, and high efficacy over conventional administration routes, laying a foundation for the transdermal drug delivery system-based treatment of rheumatoid arthritis.

Keywords Rheumatoid arthritis, Triptolide, Hyaluronic acid microneedle

Rheumatoid arthritis (RA) is a chronic autoimmune disease that can cause progressive joint destruction and associated comorbidities, including vascular, metabolic, and skeletal damage[1]. The main pathological changes involve chronic inflammation of the synovium, which leads to hyperplasia and the formation of vascular opacities that invade the cartilage. This results in the destruction of the articular cartilage and joint capsule, ultimately leading to disability due to joint deformity and loss of joint function[2]. RA is characterized by synovitis, vasculitis, and rheumatoid nodules. Vasculitis is the primary pathological basis for extra-articular manifestations, which can cause chronic skin ulceration, peripheral neuritis, and damage to multiple organs such as the lungs, heart, and kidneys[3]. A wide variety of drugs are available for the treatment of RA. The clinical approach to RA aims to alleviate pain and minimize joint damage[4]. Commonly used therapeutic agents include nonsteroidal anti-inflammatory drugs, glucocorticoids, disease-modifying antirheumatic drugs (DMARDs), and biologics[5].

Tripterygium wilfordii Hook F (TWHF) is a traditional Chinese medicine used to treat RA. Clinical preparations containing TWHF extract as the main ingredient include LeiGongTeng tablets, Tripterygium Glycosides, and LeiGongTeng sustained-release tablets. These preparations have been shown to be effective and are not prone to drug resistance[6]. Triptolide (TP) is an epoxidized diterpene lactone compound isolated from TWHF and has been shown to have anti-tumor, anti-inflammatory, and immunosuppressive effects[7]. TP is also the main toxic component of TWHF, with serious adverse effects such as hepatotoxicity, nephrotoxicity, and reproductive system damage[7]. Therefore, despite the compelling evidence supporting the application of TP for

[1]State Key Laboratory of Southwestern Chinese Medicine Resources, College of Pharmacy, Chengdu University of Traditional Chinese Medicine, Chengdu 611137, China. [2]Department of Rehabilitation Sciences, Faculty of Health and Social Sciences, Hong Kong Polytechnic University, Kowloon, Hong Kong SAR, China. ✉email: kim07.li@polyu.edu.hk; chenzhang_1990@126.com; cdutcmzjm@126.com

RA treatment, it is essential to establish an effective and safe TP delivery system for RA treatment due to its high toxicity.

Transdermal drug delivery systems (TDDS) have received considerable attention in recent years. Their advantage is that they can avoid the issues of over-elimination and poor bioavailability associated with oral drug delivery, as well as reduce systemic adverse effects of the drug. However, the passive diffusion of drugs through the skin, which is the primary protective barrier for the human body, is limited. Thus, how to safely and effectively deliver TP through the skin barrier to the target site is an important topic that needs to be investigated.

The microneedle (MN) platform offers a transdermal route for drug delivery. It has been widely used in recent years as a drug carrier for a variety of diseases, including cancer[8–10], diabetes[11–13], psoriasis[14,15], and vaccines[8,16], and even for the assessment of physiological indicators[17]. Depending on the tip material and the form of drug distribution, MNs can be classified as solid MNs, coated MNs, hollow MNs, Dissolving MNs, and hydrogel MNs[18,19]. Dissolving MNs can effectively penetrate the skin's stratum corneum and increase the amount and rate of drug transmission, and have thus become a popular research direction in TDDS in recent years[20]. They can penetrate the skin, establish drug delivery channels, and avoid contact with the nerves and blood vessels in the dermis, thus reducing pain and avoiding infection. Unlike other metal material-based MNs, dissolving MNs have a higher drug-carrying capacity and can dissolve and release loaded drugs in the skin, thus reducing the generation of medical waste[21].

Some studies have confirmed the efficacy of acupuncture, a traditional Chinese medicine therapy, for the treatment of RA, and acupuncture combined with DMARDs is often used clinically for RA treatment[22]. According to traditional Chinese medicine theory, the stomach 36 (ST36) or *Zusanli* point is abundant in qi and blood and closely linked to the pathogenesis of RA. Therefore, acupuncture at ST36 is frequently employed in traditional Chinese medicine to treat RA[23]. Zhang et al.[24] found that hand acupuncture at ST36 increased the gene levels of *PEG3*, *GADD45A*, and other tissue repair growth factors and the gene expression of the anti-inflammatory cytokine interleukin (IL)-10. It ameliorated paw redness and swelling, pain, and inflammatory cell infiltration in the joints of AIA mice. Yu et al.[25] demonstrated that acupuncture at ST36 inhibited M1 macrophage polarization and increased regulatory T cell populations to induce anti-inflammatory and analgesic effects.

The use of acupuncture in combination with drugs can suppress the toxic side effects of drugs to a certain extent, improve the bioavailability of drugs, promote the targeted movement of drugs, and improve the therapeutic efficacy of drugs. However, existing studies on the combination of acupuncture and drugs have primarily focused on the external stimulation delivered by electroacupuncture and synergistic treatment with oral drugs, and few studies have investigated the synchronous administration of drugs through acupoint stimulation[26]. Therefore, we investigated whether soluble MNs can stimulate acupoints to achieve the purpose of an "acupuncture–medicine combination".

Based on the above background, we developed a TP-loaded dissolving MN patch using hyaluronic acid and polyvinylpyrrolidone (PVP) K90 as the tip material and PVA as the backing material for the treatment of RA. A series of characterizations of the TP-loaded MNs (TP-MNs) were carried out, including the characterization of the morphology, mechanical properties, drug content, and skin insertion ability of the TP-MNs. Meanwhile, a rat adjuvant-induced arthritis (AIA) model was established using complete Freund's adjuvant (CFA), and the therapeutic effect of the TP-MNs on RA was determined by analyzing the changes in foot-plantar swelling, changes in micro-computed tomography CT images, and histology in AIA rats. The research approach is shown in Fig. 1.

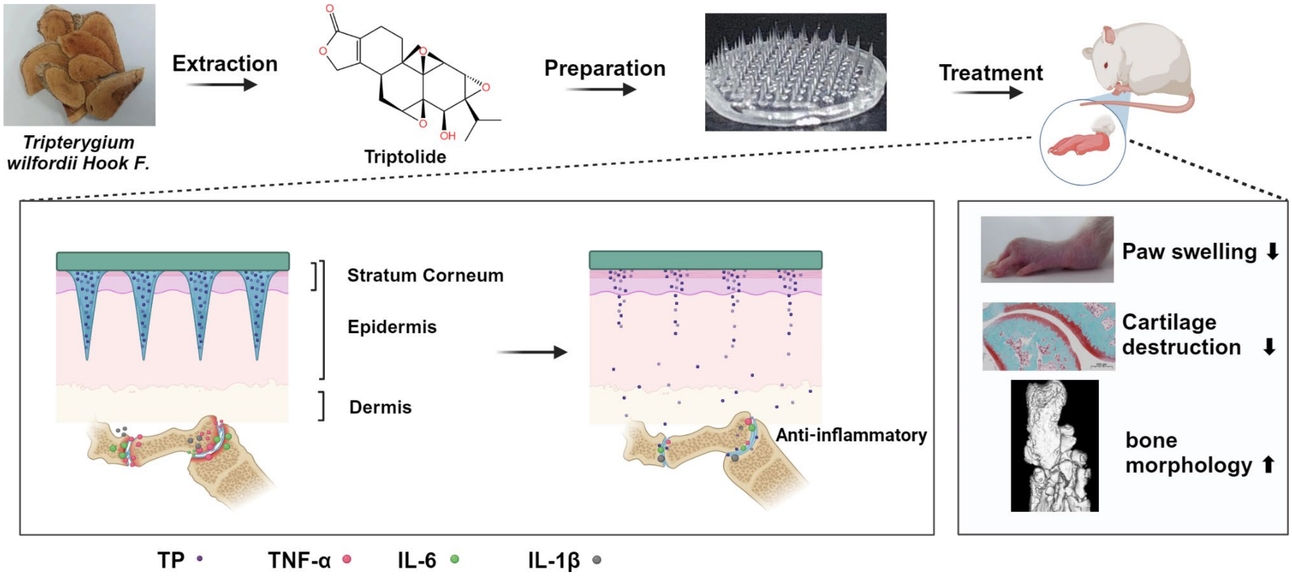

Fig. 1. Schematic showing the mechanisms outline diagram of a microneedle loaded with Triptolide for treating rheumatoid arthritis. Created with *BioRender.com*.

Materials and methods

Materials

Triptolide (TP) was obtained from Chengdu Jingcuitiancheng Pharmaceutical Technology Co., Ltd (Chengdu, China). Hyaluronic acid (HA) was provided by Shanghai Macklin Biochemical Technology Co., Ltd. (Shanghai, China). polyvinylpyrrolidone (PVP) K90 (Mw of 1300000) was purchased from Chengdu Shuobo Research and Creation Technology Co., Ltd (Chengdu, China). Polyvinyl alcohol (PVA) was supplied by Chengdu CHRON CHEMICAL Co., Ltd (Chengdu, China). 1,1′-dioctadecyl-3,3,3′,3′-tetramethylindotricarbocyanine iodide (DiR) were obtained from Dalian Meilun Biotechnology Co., Ltd. (Dalian, China). FITC was purchased from Shanghai Aladdin Biochemical Technology Co., LTD. (Shanghai, China). We obtained Polydimethylsiloxane (PDMS) molds from Taizhou Microchip Medical Technology Co., Ltd (Taizhou, China).

Animal

Male Sprague-Dawley rats weighing about 180–200 g were purchased from SPF (Beijing) Biotechnology Co., Ltd. (Beijing, China). All animal experiments involved in this study complied with the ARRIVE guidelines. The animal experiments were conducted under the permission of the Animal Ethics Committee of Chengdu University of Traditional Chinese Medicine (Chengdu, China) (permission number SYXK2020-124), all experiments were performed in accordance with relevant regulations.

Fabrication of TP-MNs

The PDMS model used to fabricate the MN arrays was provided by Taizhou Microchip Pharmaceutical Technology Co. Ltd. The MNs were conical in shape with a rounded bottom, diameter of 0.45 mm, and height of 1.2 mm. An array of 97 MNs was arranged on a circular patch with a diameter of 700 mm at a center spacing of 2 mm.

TP-MNs were divided into two layers: the drug-containing top layer and the base layer. Precisely weighed 1 mg TP dissolved in 0.5 mL of anhydrous ethanol, then sequentially added 200 mg HA, 100 mg PVP K90, mixing thoroughly so that the polymer crosslinking occurs, that is, the needle tip gel solution. TP-MNs were prepared using a two-step casting process. The tip solution was placed on the surface of the mold and defoamed using vacuum negative pressure to allow the tip solution to fully enter the voids of the mold and fill the mold, followed by scraping off the excess tip solution. Next, we added 15% w/v PVA gel solution to form the MN substrate layer by centrifuging at 3000 rpm for 5 min. Finally, after the drug-loaded molds are dried in an oven at 37–40℃, the TP-MNs are gently removed and stored dry at room temperature.

To investigate the changes in the physicochemical properties of the needle tips under different formulations, MNs without PVP K90 and TP were also prepared.

Morphological characterization

The overall shape of the finished MN arrays was observed using the eyes, and the surface morphology and rulers of the prepared MNs were examined using an optical microscope. Under vacuum conditions, gold was sprayed onto the surface of the prepared MNs, and then the three-dimensional morphology of the MNs was observed by scanning electron microscopy. Meanwhile, to clarify the distribution of the drug in the MNs as well as the 3D structure of the MNs, fluorescein isothiocyanate (FITC) was loaded into the MNs as a fluorescent probe mimicking TP, and the morphology of the MNs was imaged using a laser scanning confocal microscope (CLSM).

Determination of TP content in MNs

To determine the loading of TP in TP-MNs, the tip portion of the MNs was scraped off with a tool, and wholly dissolved with a small amount of purified water. Then extracted by adding an appropriate amount of methanol and filtered through a 0.22 μm micropore filter membrane. Subsequently, the TP content was detected using HPLC. The conditions of HPLC analysis were determined according to our group's previous research[27]. The column was used with Welch Ultimate XB-C18 (250 mm × 4.6 mm, 5 μm), the mobile phase was methanol/water (v/v, 46:54%) at a flow rate of 1.0 mL/min, and the detection wavelength was 220 nm.

Mechanical strength

The mechanical properties of MN arrays prepared by TP-MNs and other prescriptions were characterized using a texture analyzer. Briefly, the MN was placed in the center of the stainless steel plate with the tip facing upwards. Then it is necessary to adjust the distance between the tip of the MN and the sensor. Afterward, the sensor parameters were set so that the sensor was moved towards the steel plate at a speed of 0.2 mm/min, and compressive forces and displacements were measured continuously when the sensor reached the tip of the needle until the sensor moved 0.72 mm from the MN tip to the back.

Dissolution ability *in vitro*

Considering that each pinning procedure needs to be maintained for a certain period of time, we examined the *in vitro* dissolution characteristics of MN patches. The isolated skin was first prepared. SD rats were first anesthetized with isoflurane, and the rats were executed by air embolization. Next, the skin was depilated with an appropriate amount of depilatory cream, and after proper recovery, the skin was cut off and stored at -80 ℃ for use. Prior to the experiment, the skin was thawed by immersing it in a saline solution and then blotted dry with filter paper. Next, MNs were inserted into the skin with thumb pressure and fixed for different time intervals. The MN patch was then removed from the skin and observed under a light microscope.

Transdermal release ability *in vitro*

We also validated the *in vitro* release rate using Franz flow cells[28,29]. The skin containing the TP-MNs was placed on the receptor compartment and the donor chamber was installed. The receiver medium (5 mL PBS, pH 7.4, containing 0.5% Tween 80) was added to the receptor compartment to ensure complete contact of the receiver medium with the skin. It was then stirred continuously with a magnetic stirrer at 300 rpm and maintained at 37℃ in a circulating water bath. The same skin was fixed between the recipient and donor chambers and an equal amount of free TP was added as a control. Aliquots of 300 µL of receptor fluid were collected at 0, 0.5, 1, 2, 4, 8, 12, 24 and 48 h and then replaced with an equal volume of fresh dissolution medium. All samples were blown dry with nitrogen and redissolved with 100 µL methanol. Three replicate samples per group. Finally, the TP concentration was determined by HPLC (as described in Sect. "Determination of TP content in MNs") to calculate the cumulative percentage release of TP.

Microneedle insertion performance

Insertion performance in vitro

Following the methodology reported in the literature[28], we used ParafilmM to simulate skin to evaluate the insertion performance of TP-MN *in vitro*. The official website shows that the thickness of each layer of ParafilmM is 127 µm, so we folded the ParafilmM film into ten layers and fixed them on a platform. The TP-MNs were subsequently fixed to the removable test probes. Since the average force exerted by the human thumb is about 32 N[30], we fixed the TP-MN on a removable test probe, pressed the probe with the MN onto the folded ParafilmM film, applied a force of 32 N and held it for a while. Afterwards, the MN patch is removed. Use an optical microscope to observe the number of holes formed in each layer of ParafilmM film and calculate the porosity of the insert.

Insertion performance in vivo

We used SD rat's skin to test the skin insertion ability of TP-MNs. Before the experiment, the hair on the back of the rats was removed using a razor and the skin was sterilized with alcohol. After the skin had recovered for some time, we anesthetized rats with Uratan, followed by inserting MN into the skin, and kept for 5 min. Then we euthanized the rats that were still under anesthesia by removing their necks. Subsequently, the skin was quickly peeled off, fixed with 4% paraformaldehyde, paraffin-embedded, cut into 5-µm thin slices, and stained with hematoxylin-eosin (H&E) staining. Finally, the histopathologic morphology was observed under the light microscope.

Skin recovery performance

In order to assess skin recovery and the degree of irritation, we removed the MN patch after inserting it into the skin of the rat's back and keeping it in place for 10 min. Afterward, the insertion area was photographed using a camera at different time intervals until the rat skin recovered completely.

Skin penetration *in vivo*

Fluorescein isothiocyanate (FITC) was loaded in MN to evaluate the transdermal permeability of drug-loaded MN. SD rats were anesthetized and depilated, and the MN patch containing FITC was inserted into the rat skin and held for 15 min, followed by rapid removal of the skin for fixation. The skin was then quickly removed and fixed. The light was avoided throughout the procedure. The skin was scanned with CLSM to observe the depth of insertion. The skin was scanned at intervals of 8 µm until no fluorescent signal was detected, and the resulting planar images were then reconstructed in three dimensions.

In vivo pharmacodynamic study

AIA Establishment of AIA model and determination of dosing time interval

First, an AIA model was established using male Sprague-Dawley rats, and 100µL of Freund's complete adjuvant (FCA) (10 mg/mL) was injected subcutaneously into the right hind paw of rats at the dose used in the reference[31], which resulted in significant swelling of the right hind paw after 14 days. After simple skin preparation, MN patches loaded with DiR dye were applied to the site of the ST36 in rats, and the administration cycle was subsequently confirmed by observing the intensity of DiR fluorescence signals. IVIS Spectrum imager system (PerkinElmer, Waltham, MA, USA) was used to obtain images at a series of time points, including 1, 4, 8, 24, 30, and 48 h. The dosing interval would be confirmed based on the experimental results. The AIA model was established using the same method to evaluate the therapeutic effect of TP-MNs. According to the scoring and joint swelling thickness assessment[32], joint thicknesses with a score of 3 or above and 8 mm or above are considered successful in modeling. On the 14th day of modeling, rats with successful modeling were randomly divided into five groups: Model group, Free-TP group (intraperitoneal injection of free TP), Blank-MNs group (MNs without TP), Non-acupoint group (used TP-MNs at non-acupoint), and TP-MNs group (administered at the acupoint of ST36). Rats in the five groups were injected intravenously with saline, free TP, and MNs of corresponding formulations pasted at the ankle joints, and the drugs were administered once every two days for a total of ten times. The dose of TP administered in the Free-TP group was 6 µg/each, which was the same as that of TP in the drug-loaded MNs. Healthy rats without FCA induction were the normal control group ($n=6$). For administration in the MN group, the MNs were inserted with the thumb into the prepared thigh hairless skin at the location of the ST36 or at the non-acupuncture points and fixed with medical tape for 20 min to ensure that the needles were wholly dissolved.

Behavioral assessment

Before establishing the AIA model, the rats' initial body weight and right hind paw thickness were first recorded. Behavioral evaluation of the treatment effect was then performed every two days throughout the experimental period: body weight was measured to monitor the growth of the rats, while the general symptoms of the rats in each group were observed, and the degree of paw swelling was measured with a thickness gauge. The progression of inflammatory disease was also monitored using the Arthro-Index (AI) score, which quantifies the severity of RA on a scale of 0–4 based on the degree of erythema and edema[33], where 0 = normal, 1 = mild swelling and limited erythema, 2 = mild swelling and extensive erythema, 3 = moderate swelling and extensive erythema, and 4 = severe swelling and extensive erythema.

Histopathologic examination of the ankle

After ten treatments of AIA rats, SD rats were anesthetized with gaseous anesthetic isoflurane and subsequently euthanized. The right posterior ankle joint was dissected and harvested. After fixation with 4% (w/v) paraformaldehyde for 48 h, it was decalcified with 10% EDTA for a month, paraffin-embedded, and cut into thin slices. And they were stained with hematoxylin-eosin (H&E) and safranin O-fast green staining. Finally, the images of the sections were acquired using a pathology section scanner.

According to the references[34], we evaluated the changes in joint space, cartilage and bone erosion, inflammatory cell infiltration, and synovial hyperplasia in pathological tissue sections. In addition, we also scored the histopathological change of joints[35] on a scale of 0–3, where 0 = normal, 1 = mild synovitis without cartilage/bone erosion, 2 = synovitis with some edge erosion but joint structure maintenance, and 3 = severe synovitis and erosion with abnormal joint structure.

Immunohistochemical detection of ankle inflammatory factors

The section samples were labeled with antibodies against TNF-α, IL-6, and IL-1β using immunohistochemistry. After DAB staining, the brown areas were analyzed to compare the immunohistochemical results. The positive results were also analyzed semi-quantitatively using ImageJ software.

Micro-CT analysis

After treating AIA rats ten times, the rats were anesthetized and executed, the right hind ankle joint and the right paw of the rats were dissected and collected, and the muscle tissues and cartilages were dissected and fixed with 4% paraformaldehyde for 24 h. Subsequently, the bones were dried, and the difference in the bones in each group was observed using a micro-CT imaging system. Three-dimensional images of bone samples were constructed and analyzed using software to show bone trabeculae.

Safety assessment

After treating AIA rats ten times, the rats were anesthetized and sacrificed, the serum of the rats was collected, and the safety of the preparation was assessed by determining the serum levels of aminotransferase (AST), alanine aminotransferase (ALT), and the expression levels of blood urea nitrogen (BUN), and creatinine (CRE) using an autoanalyzer.

Statistical analysis

Statistical analysis was performed using GraphPad Prism 8 software. Students' t-tests and one-way ANOVA were used for statistical comparisons. A p-value of < 0.05 was considered statistically significant ($^{*}P < 0.05$, $^{**}P < 0.01$, $^{***}P < 0.001$).

Results

Characterization of TP-MNs

Morphological characterization and drug distribution

We prepared MN patch samples according to the process shown in Fig. 2A. To evaluate whether the prepared MNs had a morphology and size comparable to those of molds, we observed the morphology of the MNs by naked eye using a camera and the physical morphology of the TP-MNs using a light microscope (model) and a scanning electron microscope (SEM, Axio Imagerm2 EVO10, ZEISS, Germany). The results showed that the MN patches conformed to molds, and their tips were sharp and unbroken (Fig. 2B–D), a prerequisite for skin piercing. To observe drug distribution in the tip, FITC, instead of TP, was loaded into the MN patches and observed under an ultra-high resolution laser confocal microscope (CLSM, TCS SP8 SR, Leica, Weztlar, Germany), which showed a uniform distribution of FITC in the tip material (Fig. 2E).

After dissolving the TP-MNs in deionized water, methanol was used to extract TP, and the amount of TP extracted was determined by HPLC. The amount of TP encapsulated in each microneedle patch was 6.66 ± 0.72 µg.

Mechanical performance of TP-MNs

The tips of soluble MNs are made of polymers rather than the metals that are commonly used to make the tips of solid MNs. The mechanical properties of these polymers after drying strongly influence the ability of MNs to puncture the skin. Therefore, we investigated the effects of different material compositions on the mechanical properties of MNs. In brief, we compared the mechanical properties of different MN formulations using a texture analyzer in mechanical compression experiments. Figure 3A displays the results. The force-displacement curve indicates that the MN's compression force increased with displacement. At a displacement of 0.7 mm, a single needle's compression force reached approximately 0.15 N and 0.45 N, respectively. The MNs' insertion force required to penetrate the stratum corneum was approximately 0.098 N/needle[36]. This indicates that the MNs of

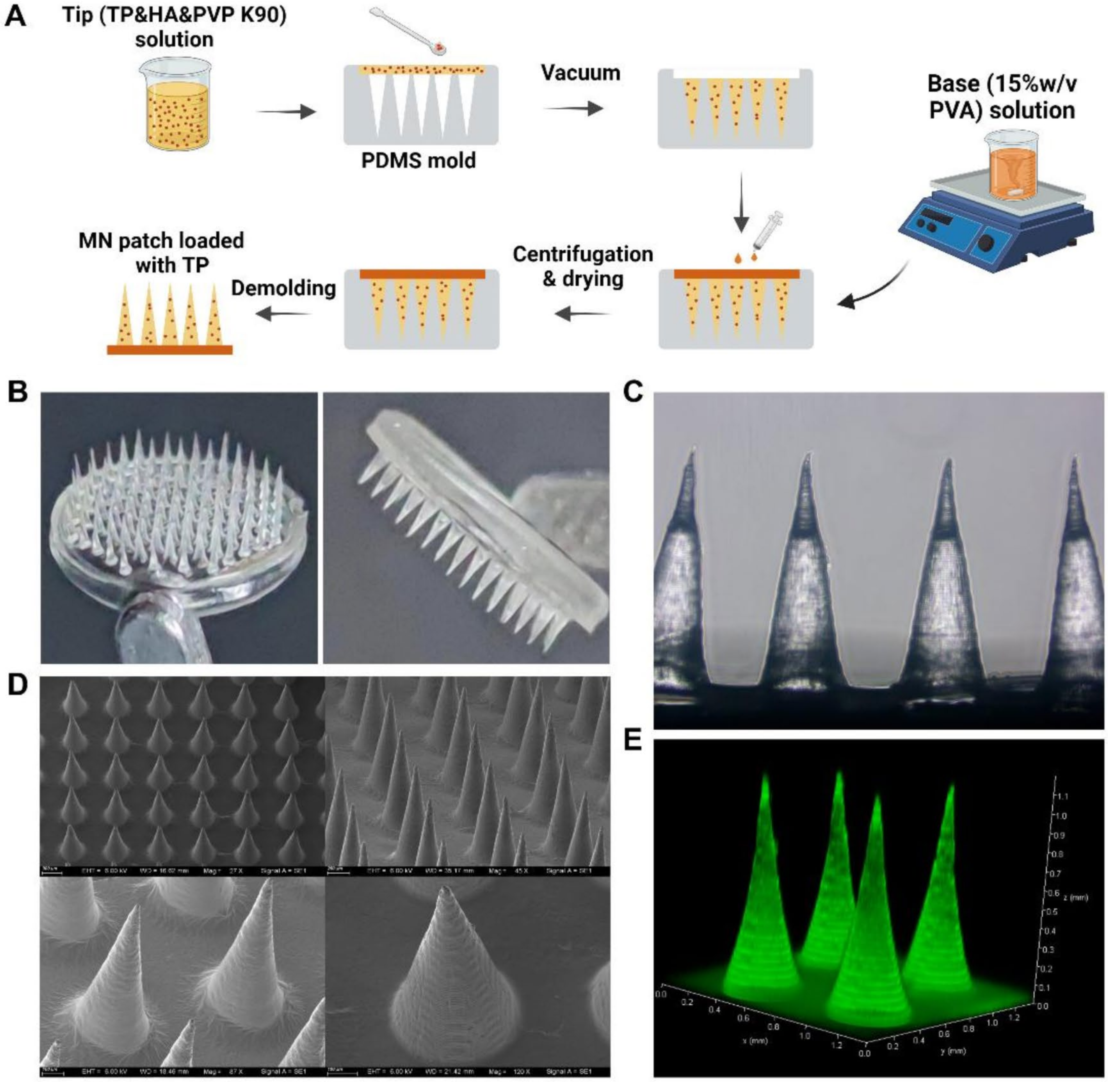

Fig. 2. Characterization of TP-MNs. (**A**) Schematic flow diagram of the preparation of TP-NMs. (**B**) Photograph of representative TP-MNs patch. (**C**) Lateral view of TP-MNs under an optical microscope, observation magnification of 10*40X. (**D**) Scanning electron microscope images of TP-MNs at different magnifications. (**E**) Side view of the 3D reconstruction of TP-MNs image by CLSM. Created with *BioRender.com*.

all of the four groups of formulations could penetrate the skin. Notably, the two groups of MNs in which PVP K90 was added to the formulation showed superior mechanical properties to the other two groups that lacked PVP K90. The addition of TP rendered slightly poorer mechanical properties, but the properties still rendered a force exceeding that required to puncture the skin. Therefore, MNs formulated with PVP K90 were used in all subsequent analyses.

In vitro dissolving property of TP-MNs

The duration of administration and stimulation in an organism is determined by the speed of MN dissolution *in vitro*. According to the literature[28], MNs with HA as the tip material can dissolve completely within 6 min of insertion due to HA's hydrophilic properties. To ensure sustained stimulation of the acupoint by the needle tip inserted into the skin tissue, we added a proportion of PVP K90. Figure 3B shows that as the MN patch containing PVP K90 was nudged over time, it gradually dissolved upon contact with tissue fluid. As anticipated, the time for the complete dissolution of the MNs increased to 15 min with the addition of PVP K90 to the needle tip.

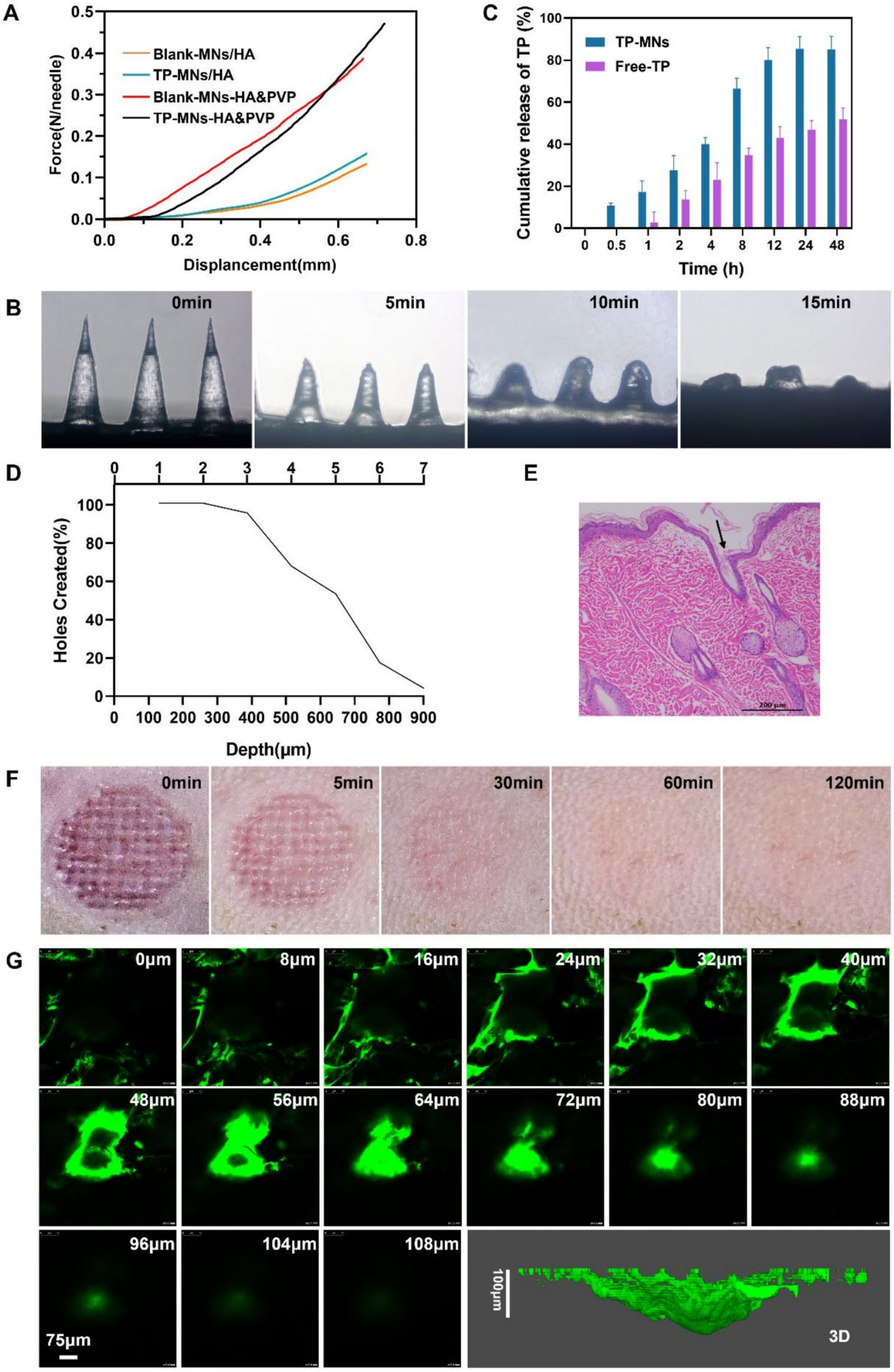

Fig. 3. Investigation of several key properties of TP-MNs. (**A**) Force-displacement curves show the mechanical properties of microneedles with different formulations. (**B**) Dissolution of TP-MNs at specified time points after application to rat skin *in vivo*. Observation magnification of 10*40X. (**C**) *In vitro* release profiles of TP-MNs and free TP during 48 h ($n = 3$). (**D**) Percentage of holes created and insertion depth of TP-MNs in ParafilmM layers. (**E**) H&E staining of skin sections to observe the depth of insertion of TP-MNs. (**F**) Recovery of rat skin at different times after application of TP-MNs. (**G**) Confocal micrographs of optical parts of rat skin at different depths *in vivo* insertion, the penetration depth was from the skin surface to a depth of 108 μm. Additionally, the representation of the three-dimensional structure generated by the insertion of FITC-loaded MNs.

In vitro transdermal release ability

The Franz diffusion cell was used to measure the *in vitro* transdermal release of TP in TP-MNs. We compared the transdermal release rates of free TP and TP MNs. *In vitro* release profiles of TP-MNs and free TP during 48 h are provided in Fig. 3C. TP in microneedles can penetrate the skin more easily, with an average release rate of 85.04% within 48 h while the permeability of free TP was 51.88%. The results showed that drug-loaded microneedles puncturing the stratum corneum of the skin increased the transdermal release of the drug compared to free TP.

Insertion properties of TP-MNs

To ensure that the MNs could withstand pressure when applied to the skin for drug delivery and successfully penetrate the skin barrier, we evaluated their insertion performance using *in vitro* and *in vivo* experiments.

First, we evaluated the insertion ability of the MNs *in vitro* using Parafilm M to simulate the skin. The results showed that all of the needle tips penetrated the first two layers of the Parafilm M membrane, and over 90% of the tips punctured the third layer, which was approximately 381 μm deep (Fig. 3D). The skin's thickness varies by body part. Generally, the epidermis is about 100–150 μm thick[37,38]. Thus, these results suggested that the MNs would be able to penetrate the epidermal barrier and deliver the drug deep into the skin.

Subsequent tests were performed on the skin of SD rats to determine the insertion depth of the MNs *in vivo*. H&E staining of skin tissue sections obtained from the MN drug delivery site showed that the MNs successfully penetrated the skin with an insertion depth of approximately 400 μm (Fig. 3E), consistent with the in vitro insertion performance. This laid the foundation for the *in vivo* pharmacodynamic study. It is important to note that the insertion depth was less than the length of the MNs due to the skin's inherent elasticity.

Skin recovery ability

Ideally, MNs for transdermal drug delivery should have excellent puncture ability without causing skin damage. Figure 3F shows that pinholes were left on the skin after MN administration, but they gradually disappeared. The puncture marks completely disappeared by 2 h post-insertion, and there was no skin reaction such as skin redness or swelling, indicating the skin was not damaged. These results indicate that TP-MNs have good biocompatibility.

In vivo penetration of drugs

To evaluate drug penetration after MN insertion, FITC was used instead of TP in the MN patch. After FITC administration, the skin tissue was removed and the vertical distribution of FITC in the rat skin was observed using ultra-high-resolution confocal microscopy. CLSM images were captured at various skin depths up to the point where fluorescence disappeared. Figure 3G shows that the fluorescence of FITC disappeared at a depth of 108 μm, indicating the MNs' ability to penetrate the stratum corneum and deliver the drug deep into the skin. The three-dimensional reconstruction image reveals that FITC diffused from the epidermis toward the dermis, following the shape of the MN. This suggests that the MN penetrated the skin after piercing it and gradually dissolved to release the drug.

In vivo pharmacodynamics in AIA rat models

Establishment of AIA rat models and timing of drug administration

The AIA rat model is a widely used classical model for studying the efficacy of anti-inflammatory drugs[39]. It is easy to manipulate, has a high success rate, and has similar immunological and pathological characteristics to humans[40]. In the present study, the AIA rat model was established by injecting 100 μL of FCA (10 mg/mL) subcutaneously into the toes of SD rats. The acute inflammatory response started 1–2 days after injection. As the inflammation progressed, the ankle and paw became significantly swollen and reddened. The swelling stabilized on the 14th day. A joint score of 3 or above and a joint swelling thickness of 8 mm or more are considered successful modeling of the AIA model.

In this experiment, fluorescent dye DiR instead of TP was encapsulated in MNs and administered to the AIA-modeled rats. The intensity of DiR fluorescence signals was measured at different time points (1, 4, 8, 24, 30, and 48 h) using an *in vivo* IVIS Spectrum imager. Figure 4A shows that a high fluorescence intensity remained at the administration site even after 48 h. Thus, 48 h was determined as the administration interval.

Behavioral evaluation and superficial observation of toes in rats

Successfully modeled rats were randomly divided into groups to study the anti-arthritic effects of TP-MNs. The experimental arrangement for the *in vivo* pharmacodynamic study is shown in Fig. 4B. Our dosing interval is once every 2 days, for a total of 10 times. Throughout the experimental period, no significant differences were observed in the body weights of rats in any group after modeling (Fig. 4C), indicating that the toe thicknesses of the rats were comparable among the groups. We measured the right hind paw thickness of the rats in each group every 2 days using a thickness gauge (Fig. 4E) to determine the degree of joint swelling and synovial inflammation. No significant difference was observed in the degree of swelling of the right hind paw in rats in the model and blank MN groups compared with healthy rats. This suggests that blank MNs had little or no therapeutic effect. TheTP-MNs group administered at the ST36 site showed slightly lower swelling in the right paw of the rats compared with the group with non-acupuncture site administration of TP. The clinical arthritis scores (Fig. 4D) were consistent with the paw thicknesses in the groups. The scores were highest in the control and blank MN groups and were not significantly different between the Free-TP group and the drug-loaded MN group. Figure 4F shows representative right claw images for each group at different time points, further confirming recovery after drug administration.

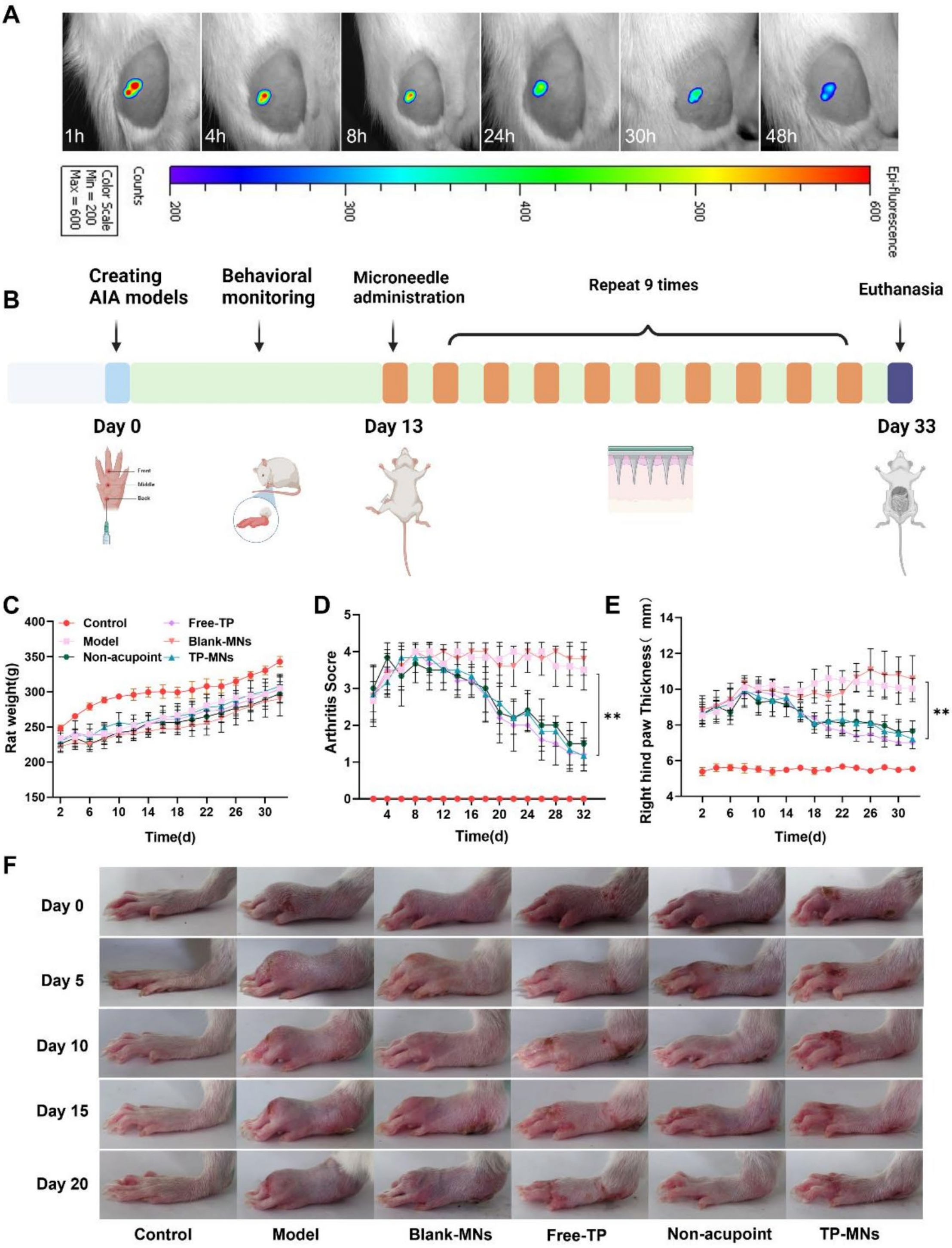

Fig. 4. *In vivo* therapeutic effects of TP-MNs on AIA models. (**A**) Establishment of dosing intervals by CLSM. (**B**) Schematic diagram of the establishment and treatment of the AIA rat model. (**C**–**E**) Body weight alterations, arthritis scores and right hind paw thickness in AIA rats (*$p < 0.05$, **$p < 0.01$, ***$p < 0.001$). (**F**) Typical images of swelling in the right hind paws of rats were taken every five days after drug administration.

Histopathological evaluation

The therapeutic effect of TP-MNs on the affected ankle joints of AIA rats was analyzed by evaluating H&E staining and safranin O-fast green staining. The H&E staining images of the model group (Fig. 5A,B) showed joint swelling, massive infiltration of immune cells, and synovial hyperplasia, indicating a severe inflammatory

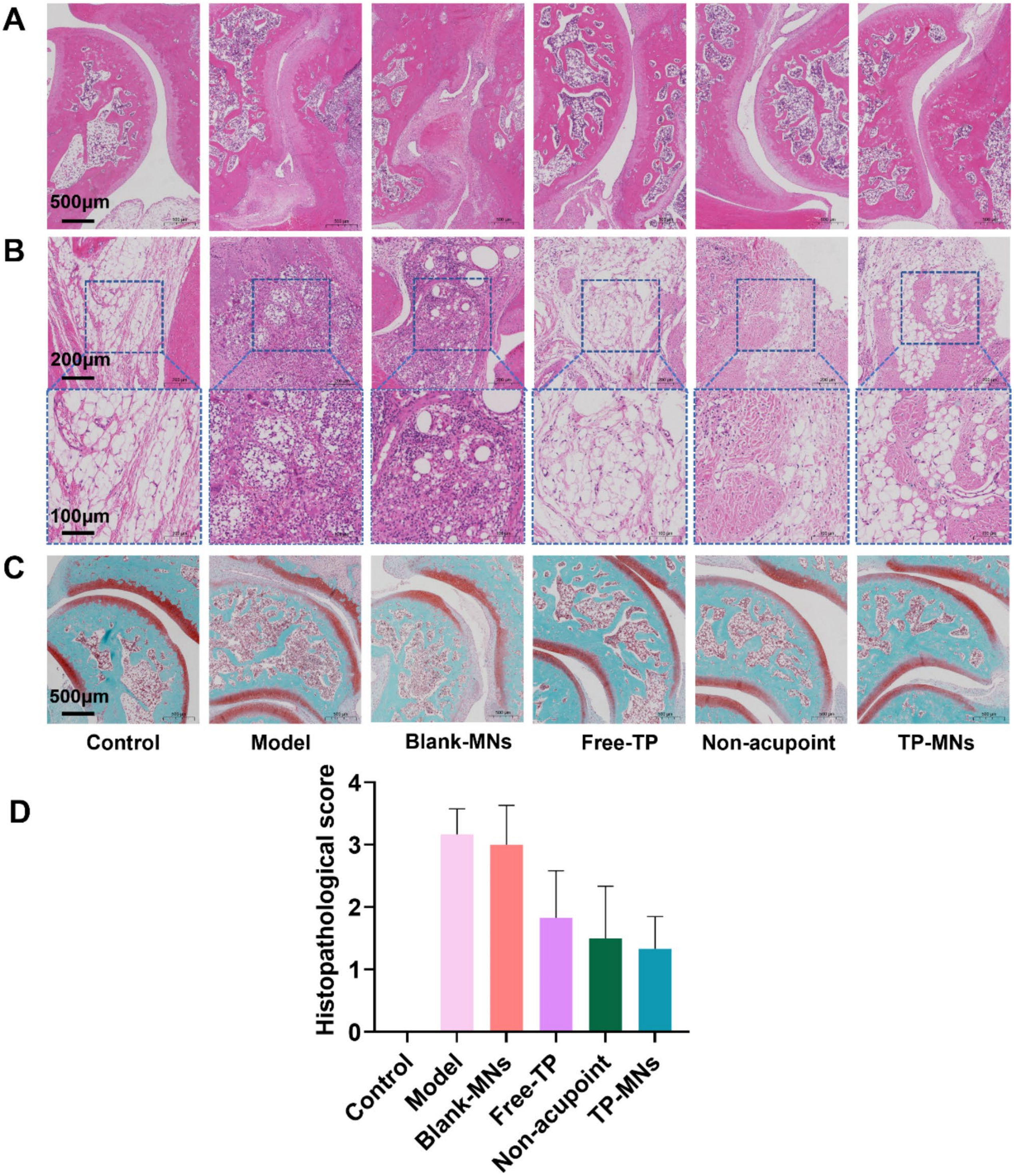

Fig. 5. Histopathological analysis of rat ankle joints. (**A**,**B**) Histopathological changes of the ankle joint and local inflammatory cell infiltration analyzed by H&E staining. (**C**) The degree of articular cartilage degeneration of the ankle joint was shown by safranin O-fast green staining in each group. (**D**) Histopathological score of rats ($n=6$).

response. The blank MN group showed no significant alleviation of the inflammatory response. In contrast, all of the three TP treatment groups showed varying degrees of reduction in inflammation compared with the model group. The safranin O/fast green-stained sections (Fig. 5C) revealed severe cartilage degeneration and bone erosion in the model group and the blank MN group. In comparison, these symptoms were significantly alleviated in the three TP treatment groups. In conclusion, the TP-MNs ameliorated the inflammatory response, joint swelling, and bone erosion in the ankle joints of AIA rats. However, no significant histopathological differences were observed between the acupoint-administered TP group and non-acupoint-administered TP group. The same result was displayed on the histopathological score of rats. Compared with the control group, the AIA model group of rats showed significant inflammatory infiltration and loss of joint structure in the ankle joint, and the joint injury degree score was significantly increased. The histopathological score of rats treated with TP MNs was the lowest (Fig. 5D).

Detection of inflammatory factors in the ankle joint through immunohistochemistry

In RA, fibroblast-like synoviocytes secrete inflammatory factors such as TNF-α, IL-1β, and IL-6[41]. These factors drive the disease process, resulting in synovial membrane hyperplasia[41], cartilage degeneration[42], and impeded bone resorption and production[43], among other effects. Reducing the expression of proinflammatory cytokines (TNF-α, IL-1β, and IL-6) in systemic and joint tissues can slow the progression of inflammation and joint damage[44].

Immunohistochemistry was used to measure the levels of the inflammatory factors TNF-α, IL-1β, and IL-6 in the affected ankle joints of rats to assess the treatment effect in each group. Figure 6A shows that the expression levels of inflammatory factors were highest in the model group and that the blank MN group was comparable to it, which is consistent with the histopathological results. In contrast, treatment with Free TP and TP-MNs effectively suppressed the inflammatory response, as evidenced by the reduced expression levels of TNF-α, IL-1β, and IL-6. Semi-quantitative analysis of the data using Image J (Fig. 6B–D) showed a significant elevation of TNF-α, IL-1β, and IL-6 levels in the model group, which were significantly reduced in the TP-administered groups. These findings suggest that TP has the potential to reduce the inflammatory response in AIA rats and that TP-MNs reduce inflammation in RA by decreasing the levels of TNF-α, IL-1β, and IL-6 in the RA-affected joints.

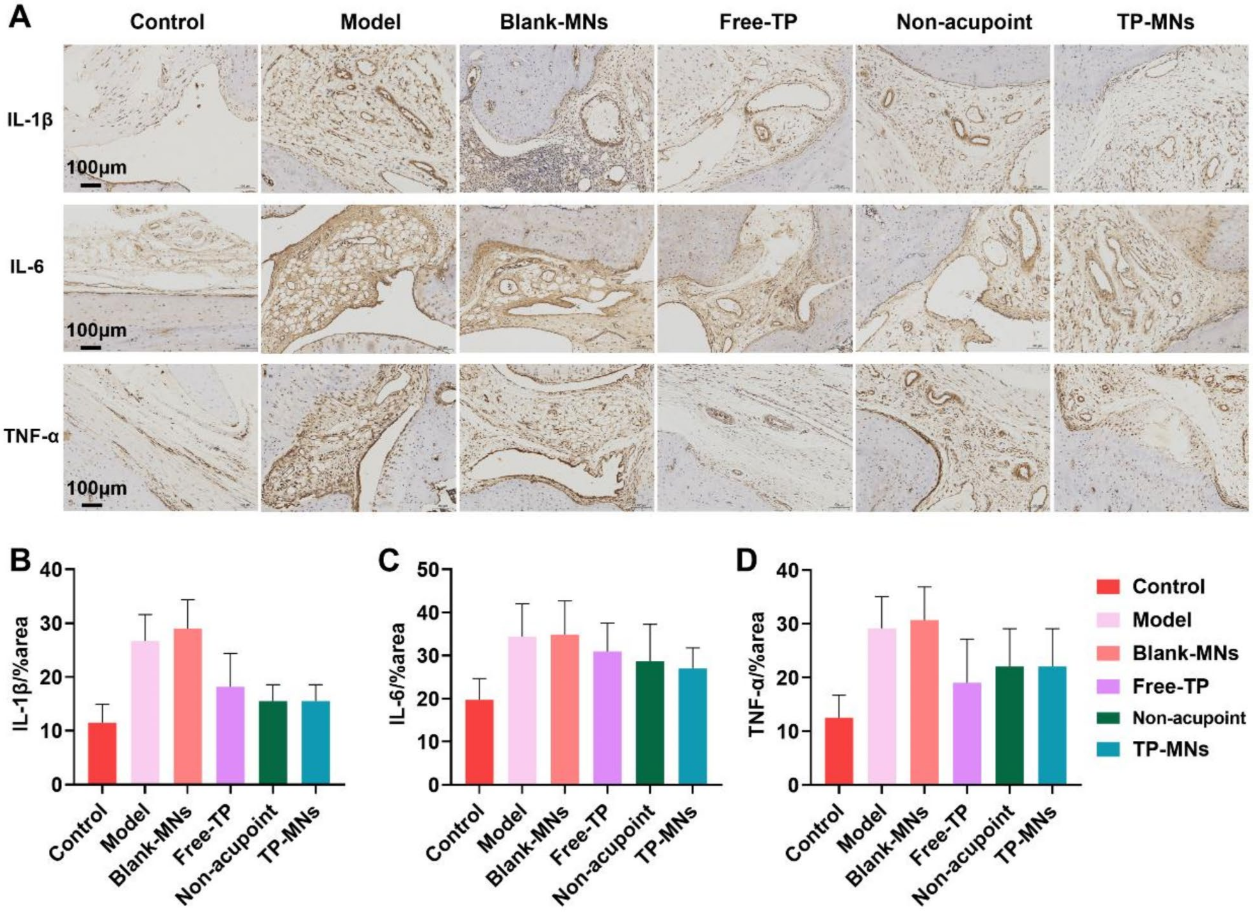

Fig. 6. Expression of inflammatory factors in the rat ankle joint detected by immunohistochemistry. (**A**) Micrographs of immunohistochemical sections of IL-1β、IL-6、TNF-α. (**B**) Semi-quantitative statistical analysis of the percentage of immunohistochemical positivity for IL-1β, IL-6, and TNF-α using Image J ($n = 6$, five areas were sampled for each sample).

Micro-CT analysis

Micro-CT was used to reconstruct three-dimensional (Fig. 7A) and two-dimensional (Fig. 7B) images of the ankle joints of AIA rats. The three-dimensional images were reconstructed for the frontal and dorsal aspects of the ankle joints, while the two-dimensional reconstructed CT images showed alterations in the morphology and structure of the bone in sagittal, coronal, and transverse planes. The bone surfaces of the control group were smooth, with a high degree of contact and tight apposition. In the two-dimensional images, well-aligned bone trabeculae were visible, and no bone erosion was observed. Conversely, in the model group, severe bone

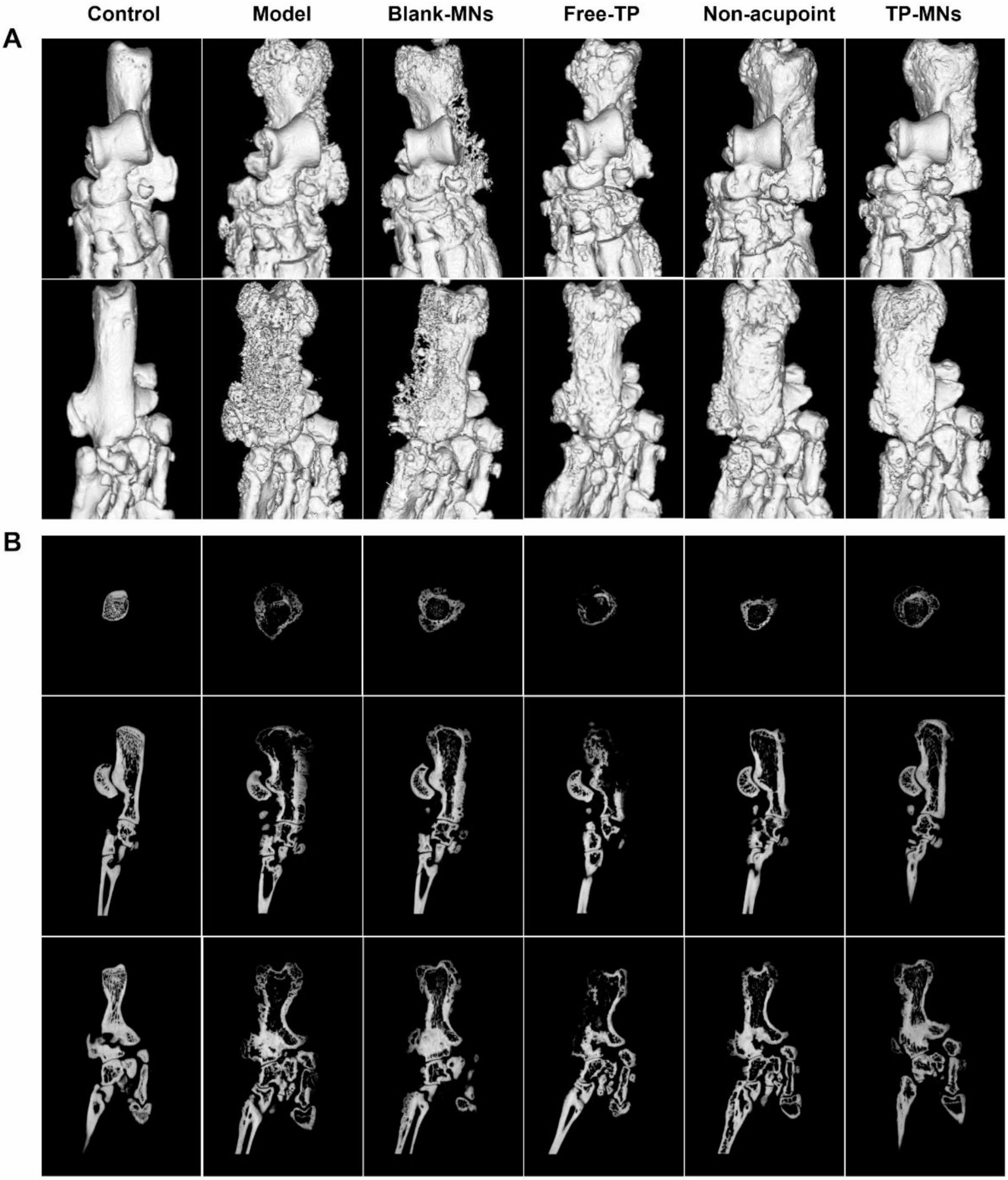

Fig. 7. Micro-CT scanning images of rat ankle joints. (**A**) Three-dimensional scanning analysis images and (**B**) two-dimensional cross-section image analysis of rat ankle joints.

	Control	Model	Blank-MNs	Free-TP	Non-acupoint	TP-MNs	*P**
ALT (U/L)	47.1	43.5	32.8	59.3	37.6	42.4	<0.0001
AST (U/L)	196.1	217.6	192.3	285.5	179.5	189.7	0.0002
BUN (mg/dL)	17.4	20.4	18.3	21.6	17.1	17.7	<0.0001
CRE (μmol/L)	47.4	47.3	48.9	66.1	57.3	52.0	<0.0001

Table 1. *In vivo* hepatorenal toxicity studies. * The average values of each group have been listed ($n = 6$). One-way ANOVA was used for statistical comparisons. A p-value of < 0.05 was considered statistically significant ($*P < 0.05$, $**P < 0.01$, $***P < 0.001$).

erosion occurred in both the front and back of the ankle joint, resulting in localized reduction of bone density and obvious destruction of the trabecular structure. In the treatment groups, all of the pathological changes were effectively alleviated. The two-dimensional images showed that the backbone erosion was reduced and the destruction of the bone trabeculae was relatively mild in the TP-MN group compared with the other TP-administered groups. These results are consistent with those of the pathological analyses.

Safety assessment

TP is known to have substantial hepatorenal toxicity. To evaluate whether local administration of TP through an MN patch can alleviate this toxicity, we performed biochemical index tests using ALT and AST as biochemical markers of liver injury and BUN and CRE as biochemical markers of renal injury to assess the safety of TP-MNs. The results showed (Table 1) that ALT, AST, BUN, and CRE concentrations were significantly increased in the Free-TP group ($p < 0.01$) compared with the other groups in which these markers were at normal levels. This result indicates that the local administration of TP using MN patches suppressed the hepatic and renal toxicity of TP, thus making MNs a relatively safe route for TP administration.

Discussion

TP is an epoxy diterpene lactone compound[45] that possesses a variety of pharmacological activities, including anti-inflammatory, immunomodulatory, and anti-tumor activities[45,46]. Studies have shown that it has clear therapeutic efficacy in the treatment of RA[47–49]. However, because of its severe hepatic and renal toxicity and narrow therapeutic window, it often causes systemic toxicity while providing therapeutic benefits[46]. Loading TP into dissolving MNs can effectively reduce the possible systemic toxicity of TP.

As a new type of drug delivery system, dissolving microneedles are convenient to use and minimally invasive[50]. Compared with subcutaneous injections, the MN-based transdermal drug delivery of TP provides a better safety profile and is more convenient[51]. The study used HA and PVP K90 as materials to prepare microneedles, which increased the permeability of TP. Although the loading amount of TP in the TP-MNs was not high, only about 6 μg/patch, it was sufficient to alter the inflammatory response in the AIA model rats. Due to the lower dosage, the liver and kidney toxicity of TP can also be effectively reduced. The study found that the prepared TP-MNs had sufficient mechanical strength to puncture the epidermis easily. *In vitro*, they dissolved within 15 min, making them suitable for simulating acupuncture needles.

Preliminary results of pharmacodynamic studies showed that all groups containing TP had anti-inflammatory and anti-swelling effects, alleviated the development of RA, improved the symptom of arthritis in AIA rats to varying degrees, reduced the degree of swelling in the toes of AIA rats, and improved the histopathological state of the ankle joints. At the same time, it could downregulate the expression of pro-inflammatory cytokines IL-1β, IL-6 and TNF-α and inhibit the inflammatory response of RA. Among them, the TP-MN and non-acupuncture groups showed the best efficacy. Unfortunately, no significant difference was found between acupoint administration (TP-MNs group) and non-acupoint administration (non-acupoint group). Acupoint drug delivery is a traditional and effective Chinese acupuncture therapy, such as moxibustion[52–54]. ST36 acupuncture has been reported to alleviate inflammation through a variety of mechanisms including vagal activation and macrophage polarization[55]. Acupuncture therapy has been used to treat rheumatoid arthritis[56]. A study showed that moxibustion at the ST36 and *Shenshu* (BL23) acupoints alleviated the pathological changes in the joints of RA rats and had a definite anti-inflammatory effect[57]. However, there are few reports on the efficacy of drugs co-delivered through MN acupuncture points. This study is the first to explore the advantages of drug delivery via MNs at acupoints. The results showed that in the group that received ST36 acupoint administration of TP-MNs, the inflammatory response characteristic of RA was alleviated to a certain extent compared with the group that received non-acupoint administration. The former group also showed a slightly better therapeutic effect in micro-CT images than the latter group, but the difference was not statistically significant. Thus, the effect of the combination of needles and drugs in the treatment of RA was not significantly better than that of non-acupoint administration of the drug. This may be due to the gradual weakening of the stimulatory effect at the acupoints after the dissolving MNs were dissolved. How to sustain the synergistic effect of the combination of needles and drugs administered using the MN drug delivery platform needs to be further explored by varying the parameters, such as increasing the dissolution time of MNs, changing the shape of MNs, or using harder matrix materials.

Conclusion

In this study, we developed a dissolving MN to deliver TP at the target site for the treatment of RA. Our findings demonstrated that the developed TP-MNs were morphologically intact and possessed sufficient mechanical strength to penetrate the stratum corneum efficiently, which significantly increased the transdermal penetration rate of TP. The intradermal dissolution rate was moderate and suitable for simulated acupuncture. *In vivo* experiments demonstrated that the TP-loaded MNs significantly alleviated paw swelling, inhibited inflammation by reducing the levels of pro-inflammatory cytokines (namely, TNF-α, IL-6, and IL-1β), and alleviated synovial destruction and reduced cartilage erosion. The transdermal administration of TP-MNs had a better safety profile and was more convenient than the traditional oral administration or intravenous injection. This study is the first to combine formulation development and acupuncture drug delivery to explore the possibility of synergistic needle–drug delivery in an RA model.

Data availability

The data that support the findings of this study are available from the corresponding author upon reasonable request.

Received: 29 July 2024; Accepted: 14 October 2024

References

1. McInnes, I. B. & Schett, G. Pathogenetic insights from the treatment of rheumatoid arthritis. *Lancet*. **389**, 2328–2337. https://doi.org/10.1016/s0140-6736(17)31472-1 (2017).
2. Rheumatoid arthritis. *Nat. Rev. Dis. Primers*4, 18002, doi:https://doi.org/10.1038/nrdp.2018.2 (2018).
3. Smolen, J. S. & Aletaha, D. Rheumatoid arthritis therapy reappraisal: strategies, opportunities and challenges. *Nat. Rev. Rheumatol.* **11**, 276–289. https://doi.org/10.1038/nrrheum.2015.8 (2015).
4. Firestein, G. S. & McInnes, I. B. Immunopathogenesis of rheumatoid arthritis. *Immunity*. **46**, 183–196. https://doi.org/10.1016/j.immuni.2017.02.006 (2017).
5. Holroyd, C. R. et al. The British Society for Rheumatology Biologic DMARD safety guidelines in inflammatory arthritis-executive summary. *Rheumatol. (Oxford)*. **58**, 220–226. https://doi.org/10.1093/rheumatology/key207 (2019).
6. Landewé, R. B. & van der Heijde, D. Comment on: 'comparison of Tripterygium Wilfordii Hook F with methotrexate in the treatment of active rheumatoid arthritis (TRIFRA): a randomised, controlled clinical trial' by Qian-Wen et al. *Ann. Rheum. Dis.* **73**, e62. https://doi.org/10.1136/annrheumdis-2014-206124 (2014).
7. Jiang, S. et al. Friend or foe? The dual role of triptolide in the liver, kidney, and heart. *Biomed. Pharmacother.* **161**, 114470. https://doi.org/10.1016/j.biopha.2023.114470 (2023).
8. Wang, C., Ye, Y., Hochu, G. M., Sadeghifar, H. & Gu, Z. Enhanced Cancer Immunotherapy by Microneedle Patch-assisted delivery of Anti-PD1 antibody. *Nano Lett.* **16**, 2334–2340. https://doi.org/10.1021/acs.nanolett.5b05030 (2016).
9. Mbituyimana, B., Ma, G., Shi, Z. & Yang, G. Polymeric microneedles for enhanced drug delivery in cancer therapy. *Biomater. Adv.* **142**, 213151. https://doi.org/10.1016/j.bioadv.2022.213151 (2022).
10. Shao, J., Li, X., Li, Y., Lin, J. & Huang, P. Self-Heating Multistage Microneedle Patch for topical therapy of skin Cancer. *Adv. Mater.* **e2308217.** https://doi.org/10.1002/adma.202308217 (2024).
11. Kim, S. et al. Implantable powder-carrying microneedles for transdermal delivery of high-dose insulin with enhanced activity. *Biomaterials*. **232**, 119733. https://doi.org/10.1016/j.biomaterials.2019.119733 (2020).
12. Zhang, X., Gan, J., Fan, L., Luo, Z. & Zhao, Y. Bioinspired Adaptable Indwelling Microneedles for Treatment of Diabetic Ulcers. *Adv. Mater.* **35**, e2210903. https://doi.org/10.1002/adma.202210903 (2023).
13. Sun, M. et al. Antibacterial microneedle patch releases oxygen to enhance diabetic wound healing. *Mater. Today Bio*. **24**, 100945. https://doi.org/10.1016/j.mtbio.2024.100945 (2024).
14. Qu, F. et al. Regulating size and charge of liposomes in Microneedles to Enhance Intracellular Drug Delivery Efficiency in skin for Psoriasis Therapy. *Adv. Healthc. Mater.* **12**, e2302314. https://doi.org/10.1002/adhm.202302314 (2023).
15. Huang, C. et al. A novel hyaluronic acid-based dissolving microneedle patch loaded with ginsenoside Rg3 liposome for effectively alleviate psoriasis. *Mater. Design*. **224**, 111363. https://doi.org/10.1016/j.matdes.2022.111363 (2022).
16. Creighton, R. L. & Woodrow, K. A. Microneedle-mediated vaccine delivery to the oral mucosa. *Adv. Healthc. Mater.* **8**, e1801180. https://doi.org/10.1002/adhm.201801180 (2019).
17. Chang, H. et al. A Swellable Microneedle Patch to rapidly extract skin interstitial fluid for timely metabolic analysis. *Adv. Mater.* **29**https://doi.org/10.1002/adma.201702243 (2017).
18. Yang, J., Liu, X., Fu, Y. & Song, Y. Recent advances of microneedles for biomedical applications: drug delivery and beyond. *Acta Pharm. Sinica B*. **9**, 469–483. https://doi.org/10.1016/j.apsb.2019.03.007 (2019).
19. Ma, G. & Wu, C. Microneedle, bio-microneedle and bio-inspired microneedle: a review. *J. Control Release*. **251**, 11–23. https://doi.org/10.1016/j.jconrel.2017.02.011 (2017).
20. Ali, M., Namjoshi, S., Benson, H. A. E., Mohammed, Y. & Kumeria, T. Dissolvable polymer microneedles for drug delivery and diagnostics. *J. Control Release*. **347**, 561–589. https://doi.org/10.1016/j.jconrel.2022.04.043 (2022).
21. Zhang, L. et al. Fabrication, evaluation and applications of dissolving microneedles. *Int. J. Pharm.* **604**, 120749. https://doi.org/10.1016/j.ijpharm.2021.120749 (2021).
22. Wan, R. et al. Comparison of efficacy of acupuncture-related therapy in the treatment of Rheumatoid Arthritis: A Network Meta-Analysis of Randomized controlled trials. *Front. Immunol.* **13**, 829409. https://doi.org/10.3389/fimmu.2022.829409 (2022).
23. Liang, F. et al. Effect of electroacupuncture at ST36 on the cerebral metabolic kinetics of rheumatoid arthritis rats. *Brain Res. Bull.* **201**, 110700. https://doi.org/10.1016/j.brainresbull.2023.110700 (2023).
24. Zhang, Y. et al. Pathological pathway analysis in an experimental rheumatoid arthritis model and the tissue repair effect of acupuncture at ST36. *Front. Immunol.* **14**, 1164157. https://doi.org/10.3389/fimmu.2023.1164157 (2023).
25. Yu, N. et al. Manual acupuncture at ST36 attenuates rheumatoid arthritis by inhibiting M1 macrophage polarization and enhancing Treg cell populations in adjuvant-induced arthritic rats. *Acupunct. Med.* **41**, 96–109. https://doi.org/10.1177/09645284221085278 (2023).
26. Chen, H. *The Pharmacokinetic Impact of oral Tripterygium gilfordii Hypaconitine by Electroacupuncture in Rheumatoid Arthritis rat Models* (Nanjing University of Chinese Medicine, 2012).
27. Xu, Z. et al. Glycyrrhizic acid-lipid Framework Nanovehicle Loading Triptolide for Combined Immunochemotherapy. *ACS Appl. Mater. Interfaces*. **15**, 41337–41350. https://doi.org/10.1021/acsami.3c08003 (2023).
28. Zhou, P. et al. Strategy for osteoarthritis therapy: improved the delivery of triptolide using liposome-loaded dissolving microneedle arrays. *Int. J. Pharm.* **609**, 121211. https://doi.org/10.1016/j.ijpharm.2021.121211 (2021).

29. Naser, Y. A. et al. Hydrogel-forming microarray patches with solid dispersion reservoirs for transdermal long-acting microdepot delivery of a hydrophobic drug. *J. Control Release*. **356**, 416–433. https://doi.org/10.1016/j.jconrel.2023.03.003 (2023).
30. Larrañeta, E. et al. A proposed model membrane and test method for microneedle insertion studies. *Int. J. Pharm.* **472**, 65–73. https://doi.org/10.1016/j.ijpharm.2014.05.042 (2014).
31. Meng, M. et al. Anti-rheumatoid arthritic effects of Paris Saponin VII in Human Rheumatoid Arthritis Fibroblast-Like synoviocytes and Adjuvant-Induced arthritis in rats. *Front. Pharmacol.* **12**, 683698. https://doi.org/10.3389/fphar.2021.683698 (2021).
32. Wang, X. et al. Anti-arthritic effect of berberine on adjuvant-induced rheumatoid arthritis in rats. *Biomed. Pharmacother.* **89**, 887–893. https://doi.org/10.1016/j.biopha.2017.02.099 (2017).
33. Heo, R. et al. Hyaluronan nanoparticles bearing γ-secretase inhibitor: in vivo therapeutic effects on rheumatoid arthritis. *J. Control Release*. **192**, 295–300. https://doi.org/10.1016/j.jconrel.2014.07.057 (2014).
34. Thao, L. Q. et al. Pharmaceutical potential of tacrolimus-loaded albumin nanoparticles having targetability to rheumatoid arthritis tissues. *Int. J. Pharm.* **497**, 268–276. https://doi.org/10.1016/j.ijpharm.2015.12.004 (2016).
35. McCann, F. E. et al. Selective tumor necrosis factor receptor I blockade is antiinflammatory and reveals immunoregulatory role of tumor necrosis factor receptor II in collagen-induced arthritis. *Arthritis Rheumatol.* **66**, 2728–2738. https://doi.org/10.1002/art.38755 (2014).
36. Yu, W. et al. Polymer microneedles fabricated from alginate and hyaluronate for transdermal delivery of insulin. *Mater. Sci. Engineering: C*. **80**, 187–196. https://doi.org/10.1016/j.msec.2017.05.143 (2017).
37. Nafisi, S. & Maibach, H. I. in *In Emerging Nanotechnologies in Immunology*. 47–88 (eds Shegokar, R., Eliana, B. & Souto) (Elsevier, 2018).
38. Lai-Cheong, J. E. & McGrath, J. A. Structure and function of skin, hair and nails. *Medicine*. **41**, 317–320. https://doi.org/10.1016/j.mpmed.2013.04.017 (2013).
39. McInnes, I. B. & O'Dell, J. R. State-of-the-art: rheumatoid arthritis. *Ann. Rheum. Dis.* **69**, 1898–1906. https://doi.org/10.1136/ard.2010.134684 (2010).
40. Grötsch, B., Bozec, A. & Schett, G. In vivo models of rheumatoid arthritis. *Methods Mol. Biol.* **1914**, 269–280. https://doi.org/10.1007/978-1-4939-8997-3_14 (2019).
41. Chen, J., Wu, W., Zhang, M. & Chen, C. Taraxasterol suppresses inflammation in IL-1β-induced rheumatoid arthritis fibroblast-like synoviocytes and rheumatoid arthritis progression in mice. *Int. Immunopharmacol.* **70**, 274–283. https://doi.org/10.1016/j.intimp.2019.02.029 (2019).
42. Mihara, M. & Hashizume, M. The effect of high molecular hyaluronic acid on the induction of matrix degradation enzymes by IL-6, IL-1β and TNF-α. *Osteoarthr. Cartil.* **20**, S134–S135. https://doi.org/10.1016/j.joca.2012.02.181 (2012).
43. Luo, X. et al. Krüppel-Like Factor 4 Is a Regulator of Proinflammatory Signaling in Fibroblast-Like Synoviocytes through Increased IL-6 Expression. *Mediators Inflamm* 1062586 (2016). https://doi.org/10.1155/2016/1062586 (2016).
44. Jain, S., Tran, T. H. & Amiji, M. Macrophage repolarization with targeted alginate nanoparticles containing IL-10 plasmid DNA for the treatment of experimental arthritis. *Biomaterials*. **61**, 162–177. https://doi.org/10.1016/j.biomaterials.2015.05.028 (2015).
45. Gao, J. et al. Triptolide: pharmacological spectrum, biosynthesis, chemical synthesis and derivatives. *Theranostics*. **11**, 7199–7221. https://doi.org/10.7150/thno.57745 (2021).
46. Xi, C., Peng, S., Wu, Z., Zhou, Q. & Zhou, J. Toxicity of triptolide and the molecular mechanisms involved. *Biomed. Pharmacother.* **90**, 531–541. https://doi.org/10.1016/j.biopha.2017.04.003 (2017).
47. de Dias, S. R. Potential therapeutic compounds from traditional Chinese medicine targeting endoplasmic reticulum stress to alleviate rheumatoid arthritis. *Pharmacol. Res.* **170**, 105696. https://doi.org/10.1016/j.phrs.2021.105696 (2021).
48. Liu, X. et al. Natural medicines of targeted rheumatoid arthritis and its action mechanism. *Front. Immunol.* **13** (2022).
49. Fan, D. et al. The Effect of Triptolide in Rheumatoid Arthritis: from Basic Research towards clinical translation. *Int. J. Mol. Sci.* **19** (2018).
50. Ita, K. Dissolving microneedles for transdermal drug delivery: advances and challenges. *Biomed. Pharmacother.* **93**, 1116–1127. https://doi.org/10.1016/j.biopha.2017.07.019 (2017).
51. Waghule, T. et al. A smart approach and increasing potential for transdermal drug delivery system. *Biomed. Pharmacother.* **109**, 1249–1258. https://doi.org/10.1016/j.biopha.2018.10.078 (2019). Microneedles.
52. Fu, L. et al. Moxibustion ameliorates osteoarthritis by regulating gut microbiota via impacting cAMP-related signaling pathway. *Biomed. Pharmacother.* **170**, 116031. https://doi.org/10.1016/j.biopha.2023.116031 (2024).
53. Jia, Y. et al. Effects of different courses of moxibustion treatment on intestinal flora and inflammation of a rat model of knee osteoarthritis. *J. Integr. Med.* **20**, 173–181. https://doi.org/10.1016/j.joim.2022.01.004 (2022).
54. Tao, S. et al. The Efficacy of Moxibustion on the Serum Levels of CXCL1 and < i > β-EP in Patients with Rheumatoid Arthritis. *Pain Research and Management* 7466313, (2021). https://doi.org/10.1155/2021/7466313 (2021).
55. Oh, J. E. & Kim, S. N. Anti-inflammatory effects of acupuncture at ST36 Point: A literature review in Animal studies. *Front. Immunol.* **12** (2022).
56. Chou, P. C. & Chu, H. Y. Clinical Efficacy of Acupuncture on Rheumatoid Arthritis and Associated Mechanisms: A Systemic Review. *Evid Based Complement Alternat Med* 8596918 (2018). https://doi.org/10.1155/2018/8596918 (2018).
57. Zhong, Y., Zhang, L., Lu, W., Shang, Y. & Zhou, H. -y. moxibustion regulates the polarization of macrophages through the IL-4/STAT6 pathway in rheumatoid arthritis. *Cytokine*. **152**, 155835. https://doi.org/10.1016/j.cyto.2022.155835 (2022).

Acknowledgements

This work was supported by Special funding from the China Postdoctoral Science Foundation (NO. 2023T160071, NO. 2021M690488); Natural Science Foundation of Sichuan Province of China for Youths (NO. 2023NSFSC1768); Science and Technology Development Fund (NO. SKL-QRCM(UM)2023–2025); The State Key Laboratory of Quality Research in Chinese Medicine, University of Macau (NO.SKL-QRCM-OP23020). The Central Guidance on Local Science and Technology Development Fund of Sichuan (NO. 23ZYZYTS0420); Multidisciplinary Evaluation of Southwest Characteristic TCM Resources Multidisciplinary Interdisciplinary Innovation Team (NO. ZYYCXTD-D-202209).

Author contributions

Siyao Li: Methodology, Investigation, Writing – original draft. Quanlong Chen: Data curation, Formal analysis. Yanglin Zhang: Visualization, Sotfware. Di Wang: Resources, Investigation. Huiling Hu: Resources, Supervision. Jingjing Li: Writing-review & editing. Chen Zhang: Project administration, Methodology. Jinming Zhang: Conceptualization, Funding acquisition.All authors reviewed the manuscript.

Declarations

Competing interests

The authors declare no competing interests.

Additional information

Correspondence and requests for materials should be addressed to J.L., C.Z. or J.Z.

Reprints and permissions information is available at www.nature.com/reprints.

Publisher's note Springer Nature remains neutral with regard to jurisdictional claims in published maps and institutional affiliations.

Open Access This article is licensed under a Creative Commons Attribution-NonCommercial-NoDerivatives 4.0 International License, which permits any non-commercial use, sharing, distribution and reproduction in any medium or format, as long as you give appropriate credit to the original author(s) and the source, provide a link to the Creative Commons licence, and indicate if you modified the licensed material. You do not have permission under this licence to share adapted material derived from this article or parts of it. The images or other third party material in this article are included in the article's Creative Commons licence, unless indicated otherwise in a credit line to the material. If material is not included in the article's Creative Commons licence and your intended use is not permitted by statutory regulation or exceeds the permitted use, you will need to obtain permission directly from the copyright holder. To view a copy of this licence, visit http://creativecommons.org/licenses/by-nc-nd/4.0/.

© The Author(s) 2024